Classification of scattering parameters of body-embedded wideband textile antennas for early diagnosis and monitoring of breast cancer

Nirmalya Das, Banani Basu [ID], Sagar Dutta and Arnab Nandi [ID]

National Institute of Technology Silchar, Silchar, Assam 788010, India

Abstract

In this paper, we propose a machine-based classification technique using the scattering parameters obtained using a wearable wideband textile antenna to diagnose breast tumors. The breast phantom is formed following the dielectric properties of the human breast tissues and characterized to ensure the resemblance with a actual tissue model for the range of frequencies from 3 to 10 GHz. A biocompatible textile antenna is fabricated and embedded on an artificial breast phantom model to capture the variation of the reflection coefficient S_{11} and the transmission coefficient S_{21} for frequencies 3–10 GHz for different locations and sizes of tumors within the phantom model. Support vector machine is used to classify the healthy tissues from the malignant tumors based on the variation of the scattering parameters owing to the variation of the dielectric characteristics of the breast phantom model. The proposed method offers 84% and 89% accuracy while using S_{11} and S_{21} parameters alone for the analysis. However, the results further improve up to 93% as a combination of S_{11} and S_{21} signals is considered.

CAMBRIDGE
UNIVERSITY PRESS

Introduction

Regular screening and early detection of breast cancer can reduce the mortality rate of the women population worldwide. In [1–3], investigation related to microwave imaging, magnetic resonance imaging (MRI)-derived three-dimensional printing technology, and thermal therapies have been carried out for early detection of tumor or breast cancer. The microwave imaging technique is inexpensive compared to MRI and low sensitivity ultrasound, and much comfortable than mammography (less sensitivity) is of great use. Tumors can be benign and malignant, as described in [4], which are thoroughly explained here. Novel techniques for the early detection of tumors can increase the quality of life and decrease the number of deaths. Joines *et al.* [5] showed tumors have a high-dielectric constant compared to healthy tissue for different frequency ranges, which becomes the main feature for breast cancer detection using microwave techniques over existing mammography and ultrasound imaging. Klemm *et al.* [6] presented a ultrawideband (UWB) microwave system for breast cancer detection with various tumor sizes. Islam *et al.* [7] proposed different antennas for microwave imaging breast cancer detection. Phantoms are basically artificial models or structure of body organs. Apart from geometrical structures, parameters like permittivity and conductivity are important for preparing phantoms. A different mixing recipe is proposed to balance the dielectric properties of a phantom model. A human breast has a relatively simple kind of structure that is easy to reproduce through simulation. Fluid glycerine [8], rubber–carbon mixture, and Triton X-100 [9] are the materials used for tissue replacement previously. Joachimowicz *et al.* [10] designed a heterogeneous phantom and measured characteristics over a 0.5–6 GHz frequency range. Lazebnik *et al.* [11] have modeled dielectric properties for normal and malignant tissues from 500 MHz to 20 GHz and 3.1–10.6 GHz using one-pole and two-pole Debye models, respectively. A muscle equivalent model designed using agar [12] is reliable for its high-melting point. Mashal *et al.* [13] developed a heterogeneous breast phantom for microwave imaging experiments using the oil–gelatin mixture, but it is very delicate in nature. Lazebnik *et al.* [14] proposed tissue mimicking phantom models for UWB applications from 500 MHz to 20 GHz. Liquid-based phantoms proposed earlier is not suitable for structures which require both interior and exterior shells to form the breast anatomy. Davis *et al.* [15] characterized breast tumor based on UWB backscatter for different sizes of tumor. An artificial intelligence method has been introduced for statistically detecting breast cancers using broadband antennas [16]. It has used dual-polarized antennas detecting tumor statistically using artificial neural networks with S-parameter inputs (S_{11} and S_{21}). Salvador *et al.* [17] has proposed an algorithm for compensating backscatter propagation and detected tumor on phantom below 1 GHz successfully. Bahrami *et al.* [18] have designed an array of flexible antennas operating from 2 to 4 GHz for breast cancer detection. Flexible antennas are suitable

for on-body application and offer robust performance at different bending radii. Datta *et al.* [19] have applied machine learning algorithm to analyze microwave signals for detecting various lower body movements using flexible antennas. Hazarika *et al.* [20] Parsha *et al.* [21] show high-gain artificial magnetic conductor- and electromagnetic band-gap-based antennas for onbody communication purposes.

In this paper, we propose machine learning-based approaches to classify the malignant and healthy breast tissues exploiting the variation of reflection and transmission coefficients of the antennas embedded on a human breast model. Three layers of heterogeneous breast phantom model with and without tumor are prepared, and the dielectric characterization is performed to resemble the live human breast tissue. A schematic of a breast phantom model is shown in Fig. 1. A flexible, biocompatible textile substrate is also characterized and used to fabricate the transmitting and receiving antennas embedded on the artificial phantom model. The S parameters of the antennas are captured and analyzed for different locations and sizes of the tumor within the breast phantom. Support vector machine, a supervised machine learning model, is exploited to classify S_{11}, S_{21}, and the combination of S_{11} and S_{21} for healthy tissues and malignant tumors at different locations with different sizes. The confusion matrix shows that the analysis based on the combination of S_{11} and S_{21} signals offers the highest accuracy of detection of malignant cells.

Dielectric properties of breast phantom

The breast tissues possess different dielectric properties (relative permittivity and conductivity) at different layers. The proposed phantom model has four constituents: skin, fat, gland, and tumor. The phantom model dielectric properties, which are frequency dependent, can be characterized by the single-pole dispersive Debye equation:

$$\varepsilon(\omega) = \varepsilon_\infty + (\varepsilon_S - \varepsilon_\infty)/(1 + j\omega\tau) - j\sigma_s/(\omega\varepsilon_0) \qquad (1)$$

$$\epsilon = \epsilon_r + i\sigma_s/(\omega\epsilon_0), \qquad (2)$$

where ϵ_r and σ_s are the frequency-dependent dielectric constant and static conductivity of the tissue, ϵ_0 is the dielectric permittivity of vacuum, ω is the angular frequency, $\sigma_s/(\omega\epsilon_0)$ is the dielectric losses, ε_∞ is the relative permittivity at high frequencies, ε_S is the static relative permittivity, and τ is the relaxation time.

Fabrication of heterogeneous breast phantom

The different layers of preparation of a phantom model is shown in Fig. 2. Three layers of the breast phantom model are prepared by mixing the constituents, as shown in Table 1. At first, the skin is prepared by mixing the constituents as mentioned in Table 1. All the materials are taken accordingly to their specific concentrations and heated in a double boiler for 5–7 min until the temperature rises to 50°C. Then they are thoroughly stirred until the temperature drops to 25°C. The mixture is placed within a bowl of 110 mm diameter and another bowl of 106 mm diameter is then pressed within it so that the skin layer achieves the required thickness of 2.1 mm. Vinegar (0.7 mL) is added as a preservative and the mixture is refrigerated overnight.

The fat is prepared using the same chemicals at different proportions and heated in a double boiler until the temperature rises
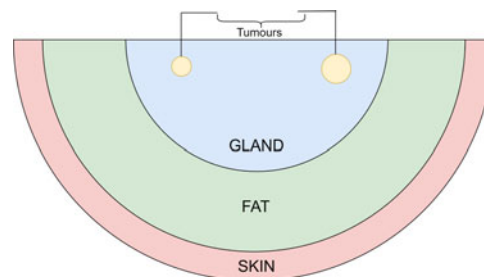

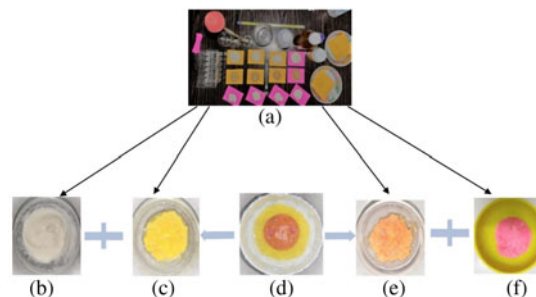**Fig. 1.** Schematic of a breast phantom.

Fig. 2. (a) Ingredients, (b) skin, (c) gland, (d) prepared phantom, (e) fat, and (f) tumor.

to 50°C. Then they are stirred until the temperature of the mixture drops to 25°C. The mixture is then emptied into the space within the skin layer. A bowl of required diameter is then pressed on it to achieve the required thickness of 33 mm.

The gland is the penultimate layer which is prepared following similar steps considering the different proportions of mixtures. The prepared solution is then emptied into the space in between the fat layer, as shown in Table 1. Straws of various diameters 5, 10, 15, and 20 mm are inserted into it and kept refrigerated overnight.

The tumor prepared by different mixtures of constituents is finally inserted into the gland using the straws of different diameters, as mentioned in Table 1.

Measurement of the fabricated phantom

The dielectric properties for different components of the phantom model are measured using a Rohde & Schwarz ZXX network analyzer via a DAK probe at 23°C. The measured values match the realistic one as showed in [22]. The detailed experimental setup is shown in Fig. 3(a). The values of the conductivity and permittivity of skin, fat, gland, and tumors for the frequency range of 3–10 GHz are shown in Figs 3(b) and 3(c), respectively. The average values of permittivity and conductivity for different components are presented in Table 2.

Antenna design

The variation of the scattering parameters of the wearable antenna proximity to the human body is investigated in the proposed work. The dispersion of the radio parameters through different layers is exploited to differentiate the malicious and healthy breast tissues. In the study, two identical antennas are designed and placed on the breast phantom model as a transmitter and a

Table 1. Breast phantom model quantities

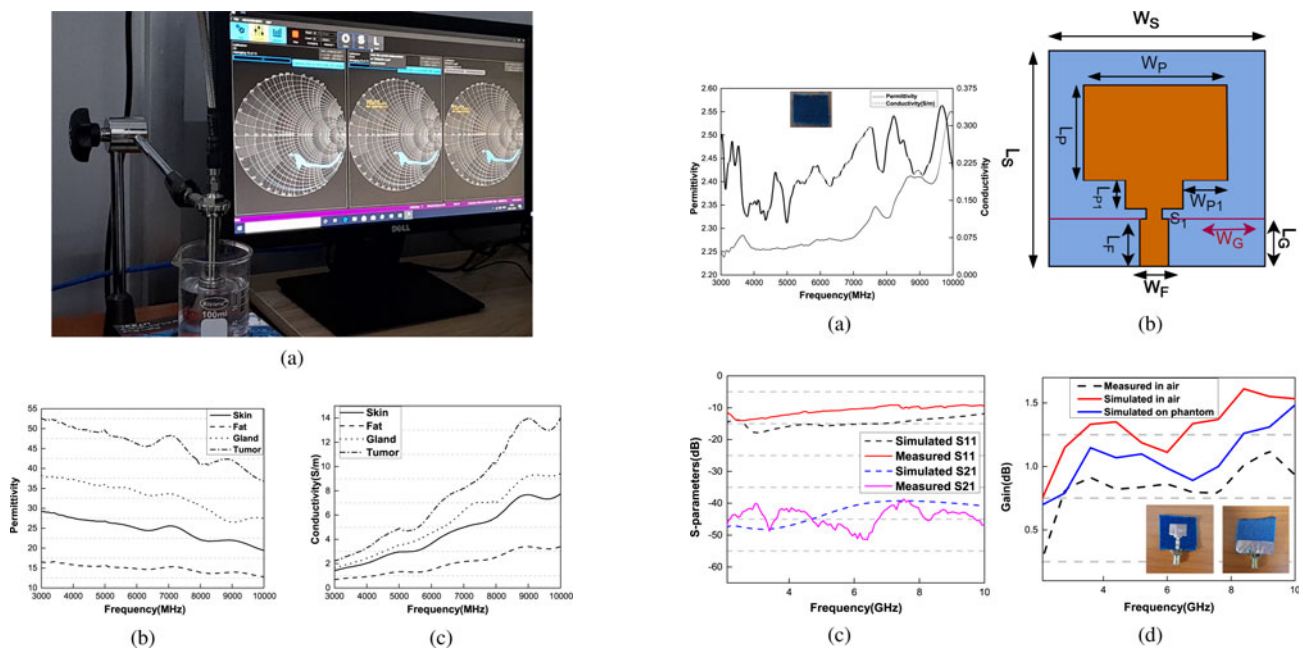| Skin	Fat	Gland	Tumor
100 mL distilled water	50 mL distilled water	70 mL distilled water	110 mL distilled water
7 mL propylene glycol	2 mL propylene glycol	7 mL propylene glycol	6 mL propylene glycol
6 g agar–agar gelatin	7 g agar–agar gelatin	5 g agar–agar gelatin	10 g agar–agar gelatin
0.7 mL vinegar	0.7 mL vinegar	0.7 mL vinegar	0.7 mL vinegar
1.5 g corn sugar gum	1.5 g corn sugar gum	1.5 g corn sugar gum	1.5 g corn sugar gum
0.7 mL liquid detergent (Ezee)	0.7 mL liquid detergent (Ezee)	0.7 mL liquid detergent (Ezee)	0.7 mL liquid detergent (Ezee)

Fig. 3. (a) Experimental setup, (b) permittivity, and (c) conductivity.

Table 2. Average values of dielectric properties of different parts of phantom model

Dielectric properties	Skin	Fat	Gland	Tumor
Permittivity (ϵ)	24.72	14.8	32.94	45.93
Conductivity (σ) (S/m)	4.52	1.97	5.51	7.77
Loss tangent (tan δ)	0.493	0.355	0.453	0.451

Fig. 4. (a) Dielectric properties of substrate, (b) antenna structure, (c) simulated and measured S_{11} and S_{21}, (d) gain of the antenna in air and on phantom, and (e) efficiency in air and on phantom.

receiver, respectively. Due to the transmission of short pulses through the breast region, the transmission and the reflection coefficient vary. The antennas exhibit a broadband behavior, and the deviations of S_{21} and S_{11} for a wide range of frequencies are recorded for the different tissue models present on the phantom. To design the textile antenna, dielectric properties of the textile substrate are characterized for 3–10 GHz frequencies using R&S ZXX material characterized and presented in Fig. 4(a). In the experiment, a denim substrate of dimensions 30 mm × 30 mm and thickness 0.8 mm is considered. The exact permittivity and conductivity are inserted in the material library of HFSS simulation software, and the UWB textile antennas resonating
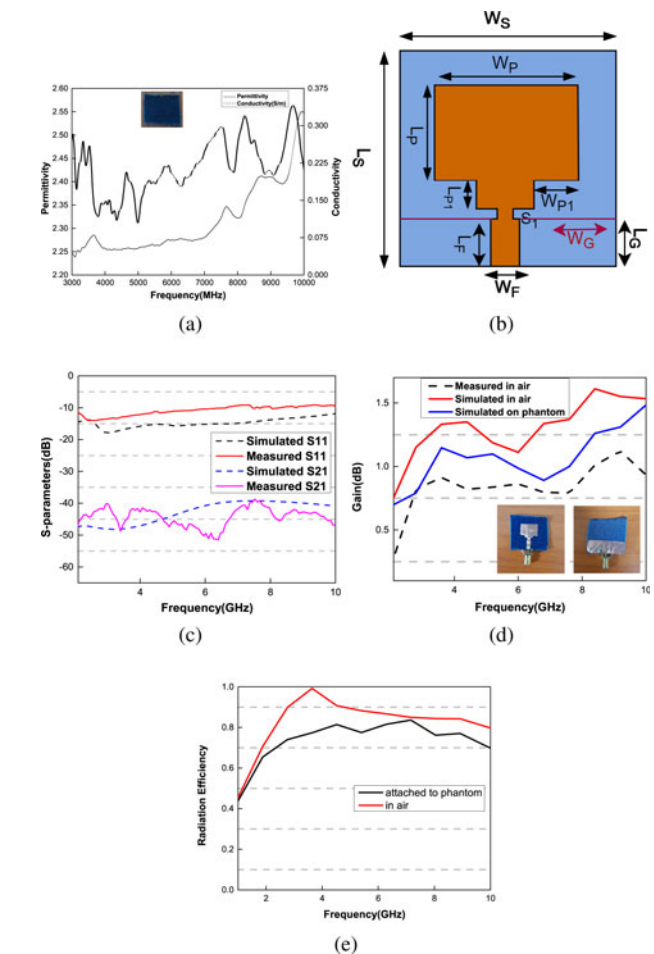
from 3 to 10 GHz are designed as shown in Fig. 4(b). The dimensions of the proposed antennas are rigorously optimized and obtained as follows: $Wp = 15$ mm, $Lp = 11.2$ mm, $Lp1 = 1.8$ mm, $Wp1 = 3.8$ mm, $S1 = 2$ mm, $LF = 10$ mm, and $WF = 3.5$ mm. A partial ground plane of dimensions $WG = 30$ mm and $LG = 10$ mm and the staircase pattern of the antenna are utilized to obtain the wide bandwidth and compact size. The simulated and measured values of reflection coefficient (S_{11}) and transmission coefficient (S_{21}) of both the identical antennas for the frequency range 3–10 GHz are shown in Fig. 4(c). The gain and efficiency of the
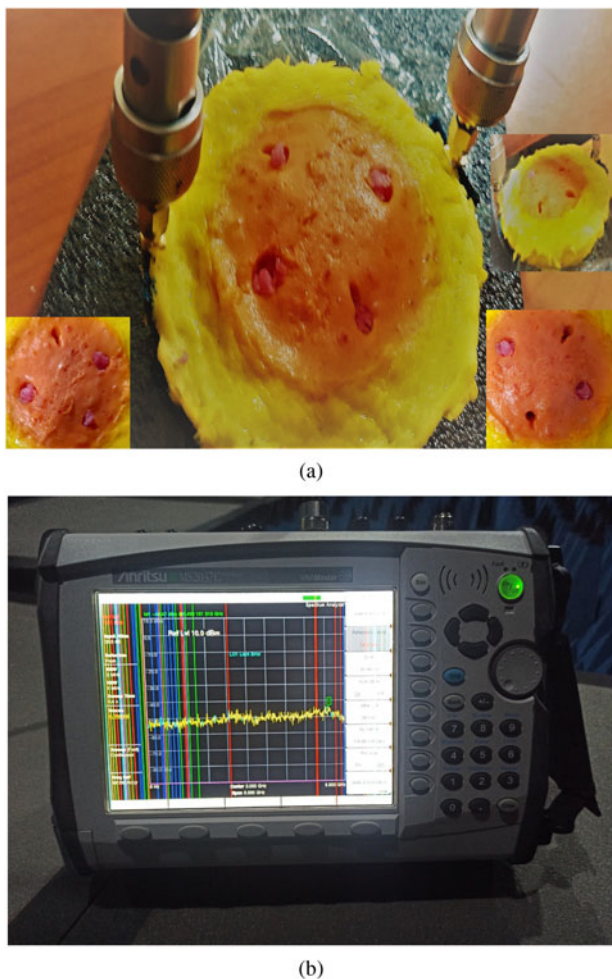
Fig. 5. (a) S_{11} and S_{21} measurement setup and (b) VNA.

Fig. 6. Flowchart of the proposed model.

antenna in air and on the phantom model are shown in Figs 4(d) and 4(e) respectively. It is seen from Figs 4(d) and 4(e) that both the parameters deteriorate when the antenna is experimented placing on the phantom model. The proposed antenna is robust and offers reasonable gain, however which is essential for capturing the deviation of scattering parameters in air as well as phantom at a wide range of frequencies due to dielectric variation.

Results and discussion

Scattering parameter measurement setup

The measurements are made using a two port Anritsu-MS2037C Vector Network Analyzer (VNA). As the maximum output power of the VNA is -3 dBm, the test antenna is fed with 0.5 mW power. For the S_{11} and S_{21} measurements, both the antennas are connected to the VNA via port 1 and port 2 and placed on or near the breast phantom model, as shown in Fig. 5. Measurements are recorded for the different positions and sizes of the tumors around the breast phantom.

Multiple data sets of S_{11} and S_{21} are created for 20 different locations of the antennas on the breast phantom with and without tumor and exploited for the classification of the tumor. In this study, we have used a support vector machine (SVM) classifier, which is a supervised machine learning model. The experiment has exploited a cubic polynomial kernel function on each data instance to map the original nonlinear observations into a higher-dimensional space in which they become separable. The box constraint level of the cubic polynomial kernel function is set at 1 for the current study. For the classification, we have utilized the classification learner toolbox in MATLAB. The workflow of the training is shown in Fig. 6.

The variation of S_{11} and S_{21} for the five cases: without tumor and with tumor of diameter 10 mm placed at four different locations are depicted in Figs 7(a)–7(e) and 8(a)–8(e), respectively. Owing to the detuning of the resonance frequency as in Fig. 7 the radiation characteristics of the antenna become affected which deteriorate the antenna gain and efficiency significantly as shown in Figs 4(d) and 4(e) respectively. Thus, the measured gain and efficiency subjected to different conditions may also be considered for the investigation. However, in this article we have studied only S_{11} and S_{21} parameters for the required analysis.

The S parameters are measured for various tumor sizes, having diameters of 5, 10, 15, and 20 mm positioned at a fixed location on the breast phantom model. Twenty sets of S_{11} and S_{22} data are recorded considering different antenna locations for multiclass classification. The variations of S_{11} and S_{21} for a specific antenna location for different tumor sizes are shown in Figs 9 and 10, respectively.
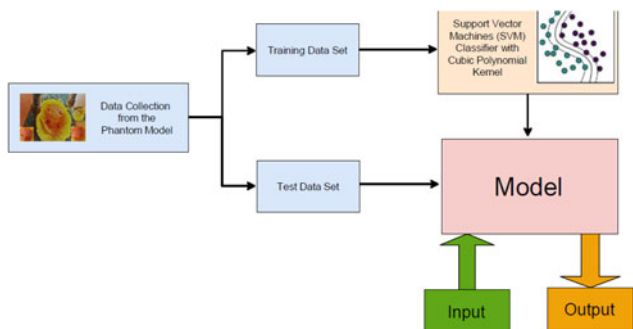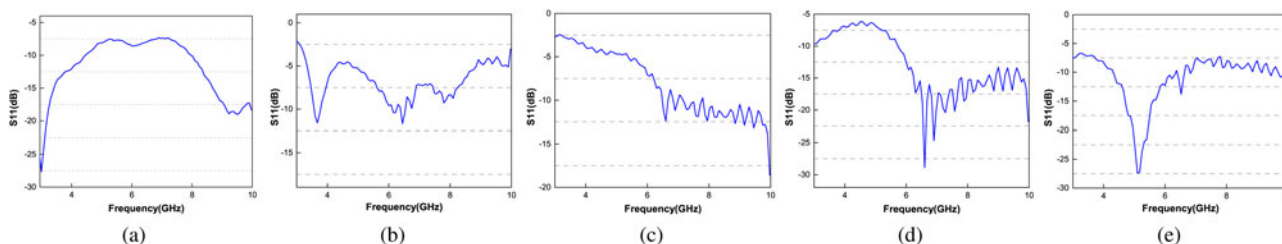

Fig. 7. Measured S_{11}: (a) without tumor and with tumor at four different locations: (b) location 1, (c) location 2, (d) location 3, and (e) location 4.
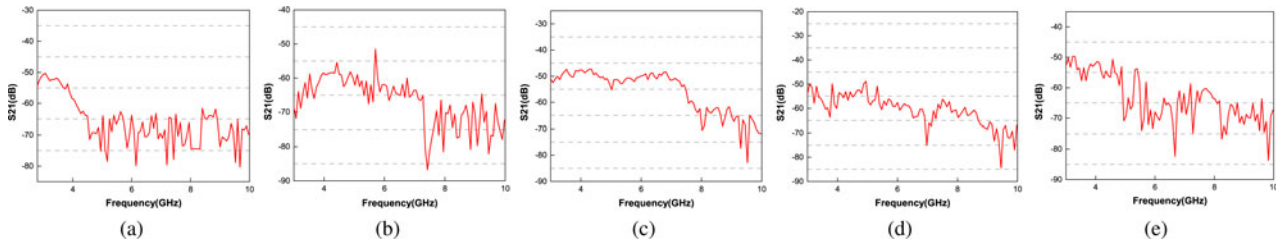
Fig. 8. Measured S_{21}: (a) without tumor and with tumor at four different locations: (b) location 1, (c) location 2, (d) location 3, and (e) location 4.
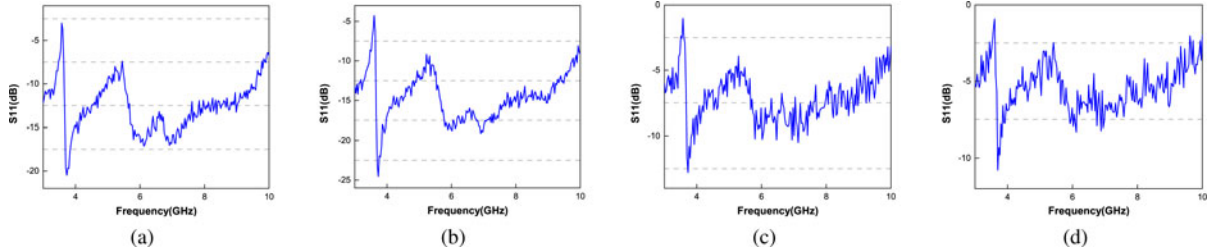

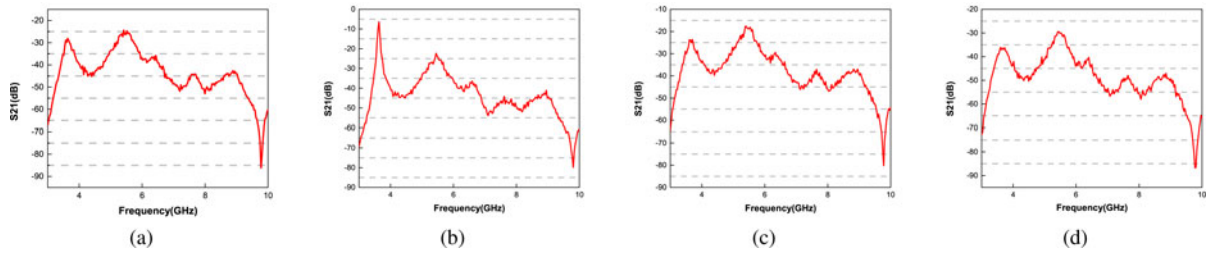**Fig. 9.** Measured S_{11} for tumor sizes (a) 5 mm, (c) 10 mm, (d) 15 mm, and (e) 20 mm.

Fig. 10. Measured S_{21} for tumor sizes (a) 5 mm, (c) 10 mm, (d) 15 mm, and (e) 20 mm.

Table 3. Features of S_{11} and S_{21} for tumors at different locations

| Parameters | Cases | Features | | | | | |
		std	rms	Mean	Peak	Clearance	Kurtosis
S_{11}	With	2.73	8.38	− 79.14	17.19	2.29	5.76
	Without	3.78	9.65	− 88.64	18.874	2.26	3.22
S_{21}	With	13.36	64.43	− 63.03	89.4	1.44	3.96
	Without	9.32	53.4	− 52.56	74.73	5.83	5.17
Both S_{11} and S_{21}	With	8.04	36.4	− 35.4	53.3	1.868	4.84
	Without	6.55	31.52	− 30.7	46.8	4.04	4.2

The statistical parameters including different features of the S_{11} and S_{21} data of the tumors at different locations and different sizes are extracted and presented in Table 3 and 4, respectively.

Figures 11 and 12 present the confusion matrix for different tumor locations and sizes of the tumors.

Table 5 presents the precision of the diagnostic for both the cases using the classifier. The data presented in Tables 5 and 6 are calculated from the confusion matrix, considering TP (true positive), FP (false positive), FN (false negative), and TN (true negative) values. It is seen that the higher the value of TP, the better the classifier is.

The 5-fold cross-validation method is used to measure the performance, which means for testing purposes, 20% of data is utilized. It is seen that as the number of features is increased, the accuracy of prediction is also increased.

Figure 13 shows the overall classification accuracy while the tumor is placed at four different locations on the breast phantom. It is seen that an average accuracy of 94% is achieved while using

Table 4. Features of S_{11} and S_{21} for tumors of different sizes

| Parameters	Cases (mm)	Features					
		std	rms	Mean	Peak	Clearance	Kurtosis
S_{11}	5	2.8751	9.5	− 8.7	12.85	1.96	6.98
	10	3.1177	12	− 9.14	13.7	2.47	5.1
	15	3.47	9.48	− 10.1	26.4	2.57	3.71
S_{21}	20	2.44	11.42	− 10.8	21.6	3.44	2.46
	5	13.71	56.4	− 62.3	92	1.29	5.13
	10	11.21	59.8	− 65.12	90.18	1.42	4.36
Both S_{11} and S_{21}	15	12.43	62	− 55	86	1.47	3.29
	20	10.04	65.3	− 64.4	80	1.55	4.24
	5	7.86	34.02	− 32.04	53	1.48	6.23
	10	6.84	36	− 34.32	61.42	2.54	4.82
	15	6.32	34.28	− 37.4	55	3.24	3.56
	20	6.82	28.84	− 33.25	51.86	2.86	3.89
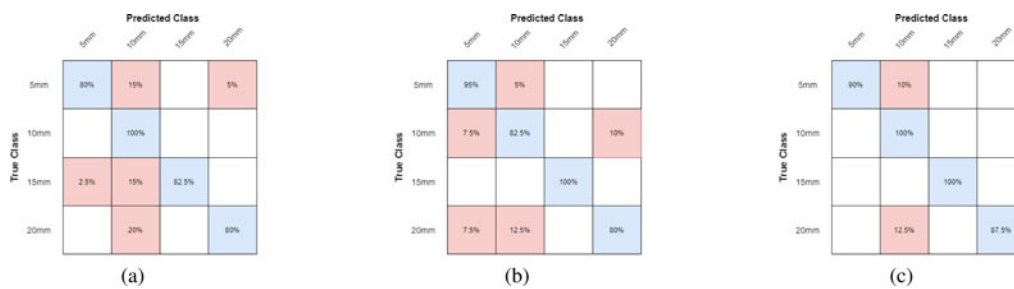
Fig. 11. Confusion matrix for different tumor sizes: (a) S_{11}, (b) S_{21}, and (c) S_{11} and S_{21}.
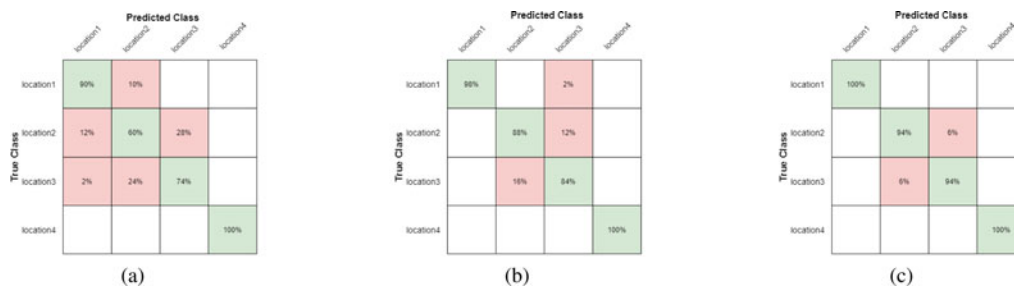

Fig. 12. Confusion matrix for different tumor locations: (a) S_{11}, (b) S_{21}, and (c) S_{11} and S_{21}.

both S_{11} and S_{21} for classification. In contrast, 84 and 89% accuracy are achieved using S_{11} and S_{21}, respectively. Alongside, Fig. 13 presents the accuracy of the proposed technique for classifying four different sizes of tumors exploiting S_{11}, S_{21}, and the combination of S_{11} and S_{22}. It is seen that an average accuracy of 94.5% is achieved while using both S_{11} and S_{21} for classification. In contrast, 84 and 89% accuracy are achieved using S_{11} and S_{21}, respectively. Along with SVM, few other classifiers like Naïve Bayes, Decision tree, k-nearest neighbors (KNN), and neural network (NN) are used for the classification and statistical performances are listed in Table 6. SVM offers superior performances in every aspect compared to that of the rest.

Specific absorption rate (SAR) analysis for the flexible textile antenna over different parts of the phantom model is performed. The average SAR value (for 1 g or 10 m) is calculated [23, 24] for different phantom parts with an input power of 100 mW. The SAR values for skin, fat, and gland are 0.0251, 0.2098, and 0.2247 W/kg, respectively, as shown in Fig. 14, which falls under the limit set by FCC and IEC standards.

Conclusion

In this paper, a machine learning approach is proposed for the classification of breast tumor based on the reflection and

Table 5. SVM classifier results

| Classifier	Different locations			Different sizes		
	S_{11}	S_{21}	Both	S_{11}	S_{21}	Both
Accuracy (%)	85.6	89.4	94.4	84	89	94
Precision	0.895	0.8925	0.955	0.855	0.925	0.95
Recall/sensitivity	0.855	0.8925	0.945	0.845	0.895	0.95
F1 score	0.86	0.89	0.945	0.82	0.9	0.945
Specificity	0.88	0.86	0.904	0.86	0.82	0.92
False positive rate	0.0892	0.0952	0.088	0.08	0.094	0.086
False negative rate	0.08	0.062	0.0526	0.06	0.082	0.0326
False discovery rate	0.1	0.08	0.0988	0.1	0.06	0.0962
Matthews correlation coefficient	0.88	0.82	0.8511	0.84	0.86	0.9
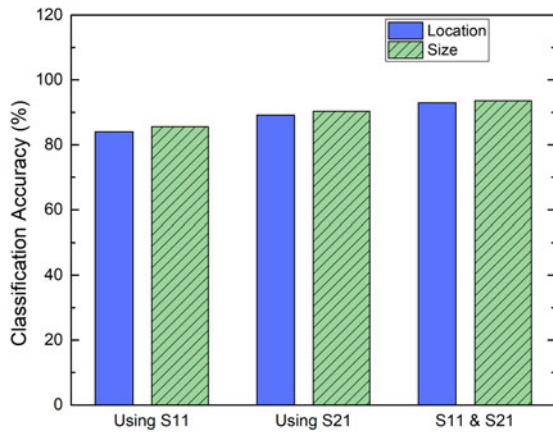
Fig. 13. Overall classification accuracy for both location and size of tumor.

transmission coefficients of the UWB antenna. The breast phantom is fabricated to match the dielectric properties of the realistic tissues. The dielectric properties of the artificial phantom layers, tumors, and the textile substrate are rigorously characterized for the entire frequency ranges from 3 to 10 GHz. The designed antenna is flexible, robust, and offers reasonably good gain over the entire band of operation and thus considered for capturing
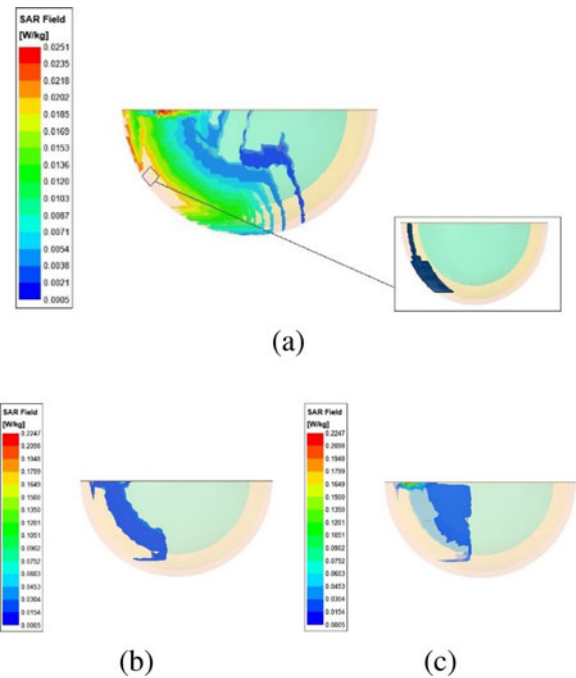
Fig. 14. SAR calculations for (a) skin, (b) fat, and (c) gland.

Table 6. Comparison with other classifiers

Classifier	For different locations				For different sizes			
	Accuracy (%)	Precision (%)	Recall (%)	F1 score (%)	Accuracy (%)	Precision (%)	Recall (%)	F1 score (%)
Naive Bayes	78.6	81.2	83	81.8	82	88	84.5	86
Decision tree	83.5	86.4	92	91.8	84.8	81.8	90.2	91
KNN	88.3	86.2	88.4	89.2	85.5	92.5	82.6	92
NN	85.3	83.01	88.05	85.8	84.8	86.2	85.3	88.2
SVM	95	93.5	89.25	94.5	94	91.8	95	94.5

the variation of *S*-parameters due to the healthy tissues and malignant cells of different sizes present at a different location within the breast model. SVM provides the highest classification accuracy of 93% as the combination of S_{11} and S_{21} are considered, but 84 and 89% accuracies as S_{11} and S_{21} are used separately. The effect of the location and size of the tumor on the classification accuracy is investigated and described in the confusion matrix statistically. For comparative evaluation, other classifiers are used, and SVM is proved to be the most accurate one. The proposed technique is inexpensive, reasonably accurate, and effective for early stage detection and continuous monitoring of breast cancer.

References

1. **Li X, Davis SK, Hagness SC, Van der Weide DW and Van Veen BD** (2004) Microwave imaging via space-time beamforming: experimental investigation of tumor detection in multilayer breast phantoms. *IEEE Transactions on Microwave Theory and Techniques*, **52**(8), 1856–1865.
2. **Burfeindt MJ, Colgan TJ, Mays RO, Shea JD, Behdad N, Van Veen BD and Hagness SC** (2012) MRI-derived 3-D-printed breast phantom for microwave breast imaging validation. *IEEE Antennas and Wireless Propagation Letters*, **11**, 1610–1613.
3. **Dabbagh A, Abdullah BJ, Ramasindarum C and Abu Kasim NH** (2014) Tissue- mimicking gel phantoms for thermal therapy studies. *Ultrasonic Imaging*, **36**(4), 291–316.
4. **Henriksson T, Klemm M, Gibbins D, Leendertz J, Horseman T, Preece AW, Benjamin R and Craddock IJ** (2011) Clinical trials of a multistatic UWB radar for breast imaging. *Loughborough Antennas & Propagation Conference*, IEEE, Loughborough University, UK. pp. 1–4.
5. **Joines WT, Jirtle RL, Rafal MD and Schaefer DJ** (1980) Microwave power absorption differences between normal and malignant tissue. *International Journal of Radiation Oncology Biology Physics*, **6**(6), 681–687.
6. **Klemm M, Craddock IJ, Leendertz JA, Preece A and Benjamin R** (2009) Radar-based breast cancer detection using a hemispherical antenna array – experimental results. *IEEE Transactions on Antennas and Propagation*, **57**(6), 1692–1704.
7. **Islam MT, Samsuzzaman M, Rahman MN and Islam MT** (2018) A compact slotted patch antenna for breast tumor detection. *Microwave and Optical Technology Letters*, **60**(7), 1600–1608.
8. **Meaney PM, Fox CJ, Geimer SD and Paulsen KD** (2017) Electrical characterization of glycerin:water mixtures: implications for use as a coupling medium in microwave tomography. *IEEE Transactions on Microwave Theory and Techniques*, **65**(5), 1471–1478.
9. **Oliveira BL, OL'oughlin D, OH'alloran M, Porter E, Glavin M and Jones E** (2018) Microwave breast imaging: experimental tumour phantoms for the evaluation of new breast cancer diagnosis systems. *Biomedical Physics & Engineering Express*, **4**(2), 025036.
10. **Joachimowicz N, Conessa C, Henriksson T and Duchêne B** (2014) Breast phantoms for microwave imaging. *IEEE Antennas and Wireless Propagation Letters*, **13**, 1333–1336.
11. **Lazebnik M, Okoniewski M, Booske JH and Hagness SC** (2007) Highly accurate Debye models for normal and malignant breast tissue dielectric properties at microwave frequencies. *IEEE Microwave and Wireless Components Letters*, **17**(12), 822–824.
12. **Kato H, Hiraoka M and Ishida T** (1986) An agar phantom for hyperthermia. *Medical Physics*, **13**(3), 396–398.
13. **Mashal A, Gao F and Hagness SC** (2011) Heterogeneous anthropomorphic phantoms with realistic dielectric properties for microwave breast imaging experiments. *Microwave and Optical Technology Letters*, **53**(8), 1896–1902.
14. **Lazebnik M, Madsen EL, Frank GR and Hagness SC** (2005) Tissue-mimicking phantom materials for narrowband and ultrawideband microwave applications. *Physics in Medicine & Biology*, **50**(18), 4245.
15. **Davis SK, Van Veen BD, Hagness SC and Kelcz F** (2007) Breast tumor characterization based on ultrawideband microwave backscatter. *IEEE Transactions on Biomedical Engineering*, **55**(1), 237–246.
16. **Woten DA and El-Shenawee M** (2008) Broadband dual linear polarized antenna for statistical detection of breast cancer. *IEEE Transactions on Antennas and Propagation*, **56**(11), 3576–3580.
17. **Salvador SM and Vecchi G** (2009) Experimental tests of microwave breast cancer detection on phantoms. *IEEE Transactions on Antennas and Propagation*, **57**(6), 1705–1712.
18. **Bahramiabarghouei H, Porter E, Santorelli A, Gosselin B and Popović M** (2015) Flexible 16 antenna array for microwave breast cancer detection. *IEEE Transactions on Biomedical Engineering*, **62**(10), 2516–2525.
19. **Dutta S, Basu B and Talukdar FA** (2020) Classification of lower limb activities based on discrete wavelet transform using on-body creeping wave propagation. *IEEE Transactions on Instrumentation and Measurement*, **70**, 1–7.
20. **Hazarika B, Basu B and Nandi A** (2021) A wideband, compact, high gain, low-profile, monopole antenna using wideband artificial magnetic conductor for off-body communications. *International Journal of Microwave and Wireless Technologies*, 1–10.
21. **Parsha MK, Nandi A and Basu B** (2021) In-band RCS reduction antennas using an EBG surface. *International Journal of Microwave and Wireless Technologies*, 1–11.
22. **Islam MT, Samsuzzaman M, Kibria S and Islam MT** (2018) Experimental breast phantoms for estimation of breast tumor using microwave imaging systems. *IEEE Access*, **6**, 78587–78597.
23. **Rao PK, Yadav AR and Mishra R** (2020) AMC-based antenna sensor for breast tumors detection. *International Journal of Microwave and Wireless Technologies*, 1–8.
24. **Subramanian S, Sundarambal B and Nirmal D** (2018) Investigation on simulation-based specific absorption rate in ultra-wideband antenna for breast cancer detection. *IEEE Sensors Journal*, **18**(24), 10002–10009.

Nirmalya Das received his B.Engg. degree in electronics and communication engineering from the Tripura Institute of Technology, Agartala, Tripura, India, in 2013, his M.Tech. degree in communication engineering from the Kalinga Institute of Industrial Technology, India, in 2015. He is currently pursuing his Ph.D. in electronics and communication engineering from the National Institute of Technology Silchar, Assam, India. His current research interests include wearable antennas, artificial intelligence, digital signal processing, and biomedical engineering.

Banani Basu received her B.Engg. degree in electronics and communication engineering from the Jalpaiguri Government Engineering College, West Bengal, India, in 2004, her M.Tech. degree in communication engineering from the West Bengal University of Technology, India, in 2008, and her Ph.D. degree in antenna array optimization from the National Institute of Technology Durgapur, West Bengal, India, in 2012. She is currently an Assistant Professor in the Department of Electronics and Communication Engineering with the National Institute of Technology Silchar, Assam, India. Her current research interests include direction-of-arrival estimation of signals and antenna array optimization.

Sagar Dutta received his B.Engg. degree in electronics and telecommunication engineering from the Gauhati University, Assam, India, in 2015 and his M.Engg. degree in telecommunication engineering from the Asian Institute of Technology, Pathumthani, Thailand, in 2017. He is currently pursuing his Ph.D. in electronics and communication engineering from the National Institute of Technology Silchar, Assam, India. His current research interests include wearable antennas, deep learning, digital signal processing, and biomedical engineering.

Arnab Nandi received his BTech degree from Kalyani Government Engineering College, India, in 2003, his MTech degree from the University of Burdwan, India in 2005, and his Ph.D. from the National Institute of Technology, Durgapur, India in 2012, all in electronics and communication engineering. Currently, he is an assistant professor in the Department of ECE, NIT Silchar, India. His research interests include ad-hoc wireless networks, wireless sensor networks, cross-layer issues, medium access control, antenna design, and artificial magnetic conductor structures.